ACS Sustainable Chemistry & Engineering

pubs.acs.org/journal/ascecg

Research Article

Piper longum Extract-Mediated Green Synthesis of Porous Cu_2O:Mo Microspheres and Their Superior Performance as Active Anode Material in Lithium-Ion Batteries

Paskalis Sahaya Murphin Kumar, Ala'a H. Al-Muhtaseb, Gopalakrishnan Kumar, Ajayan Vinu, Wangsoo Cha, Julio Villanueva Cab, Umapada Pal, and Siva Kumar Krishnan*

Cite This: *ACS Sustainable Chem. Eng.* 2020, 8, 14557−14567

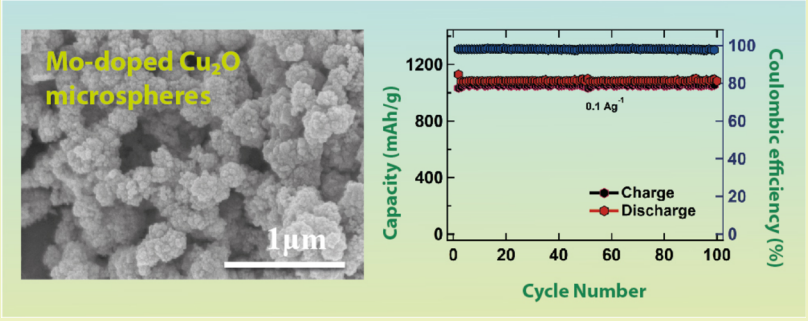

ABSTRACT: Fabrication of nano- and microstructure-based anodes capable of accommodating the lithiation-induced strain, high specific capacity, and longer cycling stability is the principal challenge for developing next-generation lithium-ion batteries (LIBs) with higher energy density. Herein, we report a green route for fabricating porous molybdenum-doped cuprous oxide (Cu_2O:Mo) microspheres of high specific surface area. The porous Cu_2O:Mo microspheres have been utilized as active anode materials in LIBs, revealing excellent electrochemical performance. The electrodes fabricated with the porous Cu_2O:Mo microspheres yielded outstanding Li-ion uptake performance, with a specific capacity of 1128 mAh g^{-1} at 0.1 Ag^{-1} and enhanced rate performance, and cycling stability (1082 mAh g^{-1} at 0.1 Ag^{-1} after 100 charge−discharge cycles). Enhanced specific capacity, stable cycling stability, and excellent rate capability of the fabricated electrodes indicate the porous Cu_2O:Mo microspheres are potential anode material for fabricating next-generation high-performance LIBs. The synthetic approach adapted for fabricating the porous Cu_2O:Mo microspheres is facile, relatively greener, and low-cost, which can be utilized for fabricating other metal oxide-based porous microstructures for application in energy storage devices.

KEYWORDS: *Cu_2O:Mo microspheres, Porous structure, Green synthesis, Anode material, Lithium-ion batteries*

INTRODUCTION

Development of efficient energy storage devices capable of operating in a cleaner and renewable way is the need of the hour to fulfill present energy demand and environment concerns.[1,2] In this perspective, rechargeable lithium ion batteries (LIBs) have demonstrated their potential for storing electrical energy at high power density. In fact, LIBs have been considered as predominant energy sources for a variety of applications including electric vehicles, energy storage grids, and portable electronic devices.[3,4] However, the principal hindrance for developing efficient LIBs is finding appropriate anode material, which plays a key role in improving the electrochemical properties of LIBs such as high energy densities, durable cycling life, and excellent rate performance.[5,6] Graphite and graphene-based materials have been widely utilized as potential anode materials for hosting Li^+ in LIBs.[7] However, the electrodes fabricated with them have relatively low intrinsic theoretical capacity (~372 mAh g^{-1}) and slow Li^+ diffusion kinetics.[7] Moreover, their lower Li^+ insertion potential (~0.1 V vs Li^+/Li), which is close to the electrochemical reduction potential of Li, is a matter of safety concern.[8] These factors severely impede the utilization of graphite and graphene-based materials in LIBs.[9] In this context, there is a growing demand for suitable alternative anode materials to overcome the aforementioned challenges. A large variety of metal oxide nanostructures have been tested as anode materials in LIBs, and some of them demonstrated

Received: July 10, 2020
Revised: August 31, 2020
Published: September 1, 2020

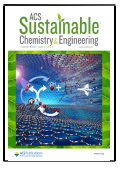

https://dx.doi.org/10.1021/acssuschemeng.0c05067
ACS Sustainable Chem. Eng. 2020, 8, 14557−14567

excellent performance with superior power density and long cycling stability.[10] However, further improvement in power density, cycle stability, charging−discharging rate, and safety concern associated with electrode materials remained as significant challenges for a breakthrough in LIBs.[11]

Numerous nanostructured metal oxides of diverse morphologies, such as manganese oxide (MnO_2),[12,13] cobalt oxide (Co_3O_4),[14] tungsten dioxide (WO_2),[15] titania (TiO_2),[16,17] silica (SiO_2),[18] tin oxide (SnO_2),[19] cupric/cuprous oxide CuO/Cu_2O,[20,21] etc. have been probed as anode materials for application in LIBs. Among the metal oxide nanostructures explored so far, nanostructures of Cu_2O[20,22,23] have attracted particular interest because of their multiple advantages including high theoretical specific capacity (∼373.9 mAh g^{-1}), moderate cost, and low-toxicity.[23] In addition, Cu_2O nanostructures reduces the over potential of Li nucleation, enabling uniform Li deposition and avoiding the formation of dendritic and dead Li. All these facts result in a high Coulombic efficiency (CE) of LIBs and improve the safety concerns by avoiding short circuits.[24] Although the Cu_2O nano/microstructures offer promising electrochemical properties, they suffer from limitations such as lower electrical conductivity and huge volume changes during charge−discharge cycles. The latter characteristic of these nanomaterials leads to severe mechanical fractures, resulting in large irreversible specific capacity loss, cycling instability, and poor rate performance in the fabricated LIBs. To overcome these issues, several strategies such as size and shape-control,[25−27] surface/interface engineering,[23] and transition metal doping[20,28] have been adapted to improve the electrochemical properties of the CuO_2 nanostructure-based anodes. Among the adopted strategies, doping of transition metal cations (e.g., Mo^{6+}, Co^{2+}, V^{5+}, Cr^{3+}, etc.) into metal oxides has been seen promising, as it improves the electrical conductivity, chemical stability, surface area, and electrochemical properties of metal oxide nanostructures.[15,29,30] Particularly, doping metal oxides with molybdenum (Mo^{6+}) has been seen to improve the electrical conductivity of metal oxides nanostructures substantially, enhancing lithium storage capacity, along with preventing their volume shrinkage during the charge−discharge process, consequently enhancing the cycling life and rate performance of these metal oxide-based LIB anodes.[31−33] Specifically, due to higher valence state of Mo^{6+} ion than Cu^{2+}, doping Mo into CuO can significantly enhance the electrical conductivity, decrease its crystallinity, induce structural distortion, and provide structural stability. All these changes have favorable impacts on the rapid Li^+ ion diffusion by shortening the Li^+ ion diffusion pathway, minimizing the volume expansion that takes places during the lithiation/delithiation process, and enhancing their capacity retention and rate capability.[34] It has been demonstrated that creation of large amounts of Cu vacancies in Cu_2O nanocrystals delivers an impressive lithium storage capability of 1122 mAh g^{-1}.[23] On the other hand, Dong et al.[31] have demonstrated a 5-fold increase in electrical conductivity of Li_3VO_4 nanostructures by incorporating Mo in V sites, which resulted in a remarkable improvement in the specific capacity and rate performance of Mo-doped Li_3VO_4 anode, revealing the crucial role of Mo doping on lithium-ion diffusivity and Li^+ ion storage capacity of LIBs. Chen et al. have also demonstrated the anode fabricated utilizing ordered mesoporous Mo-doped WO_2 in LIBs can enhance the reversible specific capacity (up to 635 mAh g^{-1}) after 70 cycles.[15] However, to the best of our knowledge, there exist no previous study on the fabrication of Mo-doped Cu_2O microstructures and their electrochemical performance in LIBs.

Over the past few years, synthesis of Cu_2O nanostructures of different morphologies has attracted considerable attention both for fundamental scientific interest and technological applications.[28] Several synthetic approaches including wet-chemical synthesis, electrochemical, hydrothermal, sol−gel, etc. have been adapted for the synthesis of Cu_2O nanostructures of different morphologies and surface structures.[20,26−28,35] However, almost all these aqueous phase chemical synthesis routes require multiple toxic solvents and surfactants, which affect our environment adversely. Due to the adverse environmental effects of toxic reagents, solvents, and surfactants in conventional chemical synthesis processes, green or eco-friendly approaches are becoming popular for the synthesis of nanomaterials.[36] Recently, synthesis of nanomaterials using plant and fruit extracts has received considerable attention, not only due to simplicity and low-cost involved in such processes but also due to increasing environmental awareness.[37,38] Specifically, piperine extract has been tested as a promising natural reductor for the fabrication of metal and metal oxide nanoparticles.[39,40] *Piper longum* belongs to the *Piperaceae* family, and it contains alkaloid piperine as well as starch, protein, saponins, carbohydrate, and amygdaline.[41] The extracted compound named piper-longumine is well recognized in medicine due to its excellent anticancer properties.[42] The presence of polyol groups or flavonoid (FlOH) contents in PLF extract plays a crucial role in the reduction of various metal precursor salts and hence the formation of their nanostructures.[43] While *Piper longum* extract has been exploited as effective medium and reductor for synthesis of metallic and metal oxide nanoparticles; however, it has not been utilized yet for synthesizing copper oxide microstructures.

In the present article, we report a simple, environmental friendly approach for controlled synthesis of submicrometric porous Cu_2O:Mo microspheres, which exhibit excellent performance as electrode material in LIBs. First, we fabricated well-dispersed submicrometric CuO microspheres of uniform sizes by reducing copper ions by *Piper longum* fruit extract under microwave irradiation at room temperature. Then, Mo-doping into CuO microspheres and subsequent reduction of CuO to Cu_2O to generate porous Cu_2O:Mo microspheres were performed by hydrothermal reaction at 180 °C. Obtained porous Cu_2O:Mo microspheres were utilized as active anode for LIBs, revealing superior electrochemical performance, and delivered a highly reversible discharge capacity of 1082 mAh g^{-1} at a current density 0.1 Ag^{-1} after 100 cycles, along with excellent rate performance.

EXPERIMENTAL SECTION

Preparation of *Piper longum* Extract. Plant dried *Piper longum* (also known as long pepper) fruits were collected, washed thoroughly several times with distilled water to clean the adhered dust particles and dried in air under the ambient conditions. The *Piper longum* fruit (PLF) extract was prepared by dispersing 0.5 g of the well-ground powder of the dried fruits in 50 mL of deionized (DI) water under magnetic stirring at room temperature for 30 min. Then, the PLF extract was obtained by filtering the solution mixture using a Whatman filter paper, and the collected PLF fruit extract was utilized for CuO microsphere synthesis.

Synthesis of CuO Microspheres. For the synthesis of CuO microspheres, first, an aqueous 2 wt % copper acetate solution was prepared by dissolving 4 g of copper acetate dihydrate [Cu-

https://dx.doi.org/10.1021/acssuschemeng.0c05067
ACS Sustainable Chem. Eng. 2020, 8, 14557−14567

$(CH_3COO)_2{\cdot}2H_2O)]$ in 200 mL of DI water and allowed to magnetically stir for 30 min. Then, in the glass beaker containing the copper precursor salt solution, 30 mL of the PLF extract was added under magnetic stirring at ambient temperature, which resulted in a color change of the reaction mixture from light blue to light green (Figure S1, Supporting Information). Then, this reaction mixture-containing glass beaker was then subjected to microwave heating at 540 W for 10 min in a commercial microwave oven (Whirlpool 0.5 cft countertop microwave oven, WMC20005YD). The formed brownish-black precipitate at the bottom of the reaction beaker was filtered, washed thoroughly using DI water and ethanol for at least three times, and dried at 80 °C for 2 h. For comparison, CuO microparticles were also synthesized without assistance of the PLF extract, maintaining all other conditions the same as CuO microparticle synthesis, and the sample was denoted as CuO_P.

Synthesis of Porous Mo-Doped Cu_2O (Cu_2O:Mo) Microspheres. In a typical synthesis, 50 mg of as-synthesized CuO microspheres was added into 50 mL of DI water under magnetic stirring for 30 min to obtain a well-dispersed colloidal suspension. Then, a mixture of 5 mmol of ammonium heptamolybdate tetrahydrate $(NH_4)_6Mo_7O_{24}{\cdot}4H_2O$ and 17 mmol of citric acid monohydrate $(C_6H_8O_7{\cdot}H_2O)$ was slowly added to the colloidal solution under magnetic stirring for 30 min. The obtained solution mixture was then transferred into a 100 mL Teflon-lined autoclave and heated at 180 °C for 12 h inside of an oven. After cooling down to room temperature, formed black precipitate was separated by centrifugation (at 3000 rpm for 20 min), washed thoroughly at least 3 times with DI water and ethanol each, and dried at 80 °C for 6 h, obtaining porous Cu_2O:Mo microspheres in powder form.

Characterization of CuO and Porous Cu_2O:Mo Microspheres. Formation and crystallinity of the fabricated microspheres were analyzed in an X'Pert PRO PANalytical powder X-ray diffractometer (XRD) using monochromatic Cu K_α X-rays (λ = 0.15406 nm) in the 2θ angle range from 20° to 80°. Surface morphology and the elemental composition of the prepared samples were examined using a field emission scanning electron microscope (FESEM, Hitachi SU800) equipped with X-ray energy dispersive spectrometer (EDS) at operating voltage of 5 kV. The microspheres of the as-prepared samples were analyzed using a Joel 2100F transmission electron microscopic (TEM) microscope (JED2300T, JEOL) operating at 120 kV. For TEM measurements, the samples were prepared by dispersing the synthesized powder samples in ethanol and then the colloidal suspension was deposited over carbon-coated Cu grids and drying at ambient condition. The specific surface area (SSA) and pore-size details of the samples were acquired from nitrogen (N_2) adsorption–desorption isotherms at liquid nitrogen temperature (77 K) using micrometrics ASAP 2020 (NIMS, Japan) sorbtometer after degassing them at 180 °C for 3 h. Elemental composition of the samples and chemical oxidation states of their constituting elements were examined using a PHI Quantera II X-ray photoelectron spectrometer (SXM, ULVAC-PHI, NIMS, Japan) utilizing Al Kα X-ray source (1.4 mm × 0.1 mm, 100 W, 20 kV, 5 mA) and hemispherical electron analyzer (ECALAB MKIV). Electrical properties of the samples were conducted in a Zive MP2 electrochemical impedance spectrometer (EIS) using a multichannel electrochemical workstation.

LIB Application of Porous Cu_2O:Mo Microspheres. For electrochemical analysis, the anode electrodes were fabricated by mixing 75 wt % active material (CuO, and Cu_2O:Mo microspheres) with 15 wt % acetylene black (AB) and 10 wt % poly(acrylic acid)-carboxymethyl cellulose. The slurry was spread over a cleaned commercial copper sheet (Sigma-Aldrich, 99.0%), dried at 120 °C in a vacuum oven overnight, and then pressed well in order to increase the connectivity between the anode material and copper current collector. The area of the fabricated electrodes was about 1.539 cm^2, and the active material mass loading was about 1.0–1.5 mg cm^{-2}. The LIB battery cells were assembled utilizing the 2032 standard battery coin cells inside an air-filled glovebox. A mixture of 1 M $LiPF_6$ in an ethylene carbonate (EC) and dimethyl carbonate (DMC) mixture was employed as electrolyte, and a thin polypropylene membrane was used as a separator. Lithium metal foils were utilized as counter and reference electrode. All the electrochemical measurements such as charge–discharge tests were carried out in a Zive MP2 (Seoul, South Korea) multichannel electrochemical workstation.

RESULTS AND DISCUSSION

Synthesis and Characterization of Cu_2O:Mo Microspheres. As has been shown schematically in Figure 1, we

Figure 1. Schematic illustration of the two-step synthesis process utilized for fabricating porous Cu_2O:Mo microspheres.

fabricated Cu_2O:Mo microspheres in two steps. In the first step, uniform CuO microspheres were prepared using a green approach via microwave irradiation-assisted reduction of copper acetate precursor in *Piper longum* fruit extract, which serves both as a solvent and as reducing agent. Moreover, due to the presence of long-chain piperine, it also works as a surfactant for the controlled growth of the CuO microspheres. Specifically, the flavonoid (FlOH) contents present in the PLF extract, which act as a mild-reducing agent for the slow reduction of copper acetate precursor salt along with subjection of microwave irradiation, lead to controlled growth of CuO microspheres.[39,44] The PLF extract plays a dual role as solvent and slow-reductor for the growth of CuO microspheres. The CuO microparticles was also obtained without assistance of PLF extract, keeping other synthesis conditions unchanged, which generated irregular spherical particles (Figure S2, Supporting Information), clearly demonstrating the role of PLF extract as reductant and shape-directing agent for the growth of CuO microspheres. In the second step, Mo doping and subsequent formation of porous Cu_2O microspheres was accomplished via hydrothermal treatment at 180 °C for 12 h, where the presynthesized CuO microspheres was reduced Cu^{2+} ions into Cu^+ and reduced Cu^+ can partially over reduced to Cu^0.[45] The average Shannon radii[46] of MO^{6+} ions (0.41 Å) and Cu^{2+} is about 0.73 Å, respectively.[47] As the ionic radius of Cu^{2+} is relatively higher than that of MO^{6+}, the replacement of Cu^{2+} by Mo atoms is highly feasible in the host lattice. In fact, a similar doping mechanism has been proposed for several transition metal cations of different ionic radii in metal oxides.[15,33,48,49]

Crystallinity and phase purity of the as-synthesized pristine CuO and Cu_2O:Mo microspheres samples were investigated by powder X-ray diffraction (XRD) analysis. The XRD patterns of the pristine CuO, Cu_P, and porous Cu_2O:Mo microspheres samples are presented in Figure 2. All the diffraction peaks appeared for the pristine CuO and CuO_P

https://dx.doi.org/10.1021/acssuschemeng.0c05067
ACS Sustainable Chem. Eng. 2020, 8, 14557–14567

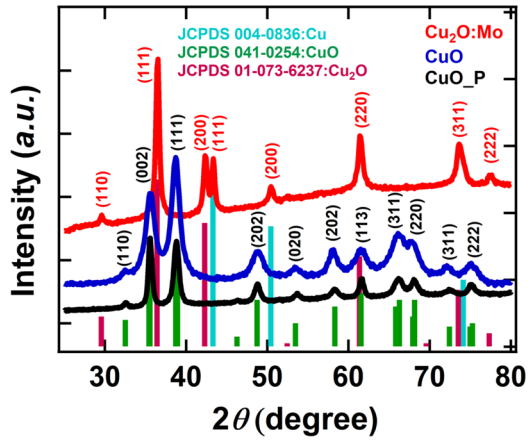

Figure 2. Typical XRD patterns of the CuO, CuO_P, and Cu_2O:Mo microspheres.

samples at 2θ = 32.5, 35.51, 38.73, 48.8, 58.31, 67.73, 68.14, 72.43, 83.3° could be indexed to the (110), (002), (111), (202), (020), (202), (113), (311), (220), (311), and (222) planes of monoclinic CuO (JCPDS card no. 041-0254).[44] In the case of the Cu_2O:Mo sample, there appeared diffraction peaks at 2θ = 29.6, 36.4, 42.2, 61.3, 73.5, and 77.3°, which could be indexed to the (110), (111), (200), (220), (311), and (222) planes of crystalline Cu_2O in the cubic phase (JCPDS card no. 01-073-6237). The observed XRD diffraction peaks positions are consistent with the previously reported values for Cu_2O.[50,51] There appeared three additional diffraction peaks at 2θ = 43.3, 50.4, and 74.0° in the latter sample, which corresponded to the (111), (200), and (220) planes of Cu^0 (JCPDS card no. 00-004-0836).[52] The XRD result confirms that the conversion of CuO to Cu_2O and along with a partial reduction of Cu_2O to Cu^0 during hydrothermal treatment in the presence of citric acid.[52] However, the Cu_2O phase was the dominant phase in the resultant Cu_2O:Mo sample as evidenced in its XRD pattern. It should be noted that there appeared no signal corresponding to metallic phase of Mo or Mo oxides in the diffraction pattern of Cu_2O: Mo. However, a slight shift in the diffraction peaks of Cu_2O toward a higher degree was observed, suggesting the possible doping of Mo atoms into the Cu_2O lattice.[47]

Morphology of the as-synthesized samples was investigated by SEM and TEM analysis. Figure 3 displays typical SEM images of the pristine CuO and Cu_2O:Mo microsphere samples. As can be noticed in Figure 3a,b, the pristine CuO sample consists of well-dispersed spherical microspheres of 500−700 nm size range (Figure S3, Supporting Information). Each of these spherical microspheres are composed of tiny assembled nanoparticles (NPs). On the other hand, SEM images of the as-synthesized CuO_P microparticles (prepared without PLF extract) are shown in Figure S2 (Supporting Information), which showed their nonuniform spherical morphology with size varying between 500 and 800 nm. The SEM images of the Cu_2O:Mo sample (Figure 3c,d) revealed the formation of spherical, highly porous particles of 200−250 nm sizes with uneven surfaces. Such a significant size reduction and morphology change of the particles in Cu_2O:Mo are the indications of Mo incorporation into the pristine CuO microspheres, and their successful conversion to Cu_2O:Mo. The results also evidence that the Mo doping into CuO microspheres causes significant structural distortion and reduction in the particle size.

Figure 4 shows typical low- and high-resolution TEM (HR-TEM) images of the Cu_2O:Mo microspheres sample along with elemental distribution in them. As can be noticed in the low-resolution TEM images presented in Figure 4a,b, the sample consists of 200−250 nm diameter particles formed by the assembly of smaller, densely connected primary particles. The HR-TEM image in Figure 4c shows the appearance of well-defined lattice planes, indicates the primary nanoparticles bear good crystallinity. The estimated interplanar distance of 0.30 nm corresponds well with the interplanar spacing of (110) planes of Cu_2O lattice.[53] Doping of Mo in the Cu_2O was also confirmed through EDS elemental mapping of the porous Cu_2O:Mo microsphere sample. As shown in Figure 4d, all the elements (Cu and O, Mo) remained uniformly distributed in the microspheres. Furthermore, the EDS-elemental analysis spectrum (Figure 5a) confirms that the detection of Cu, Mo,

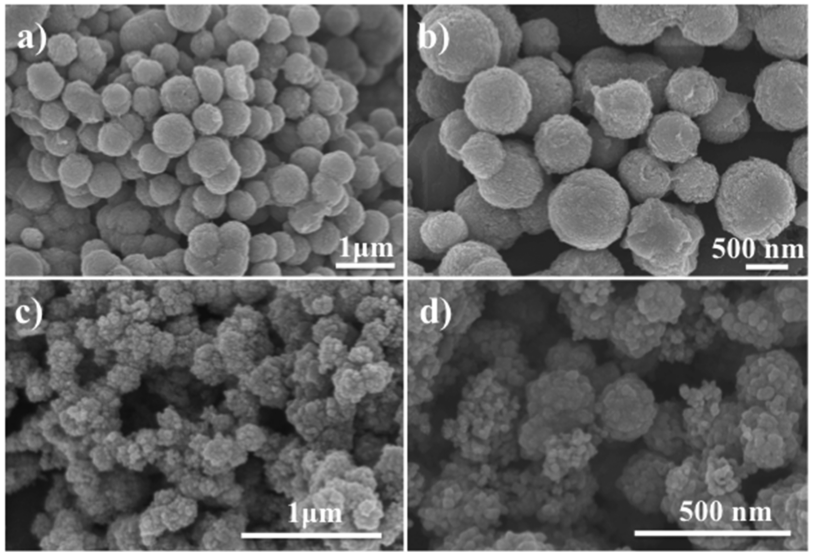

Figure 3. Typical low- and high magnification SEM images of as-synthesized CuO microspheres (a, b), and porous Cu_2O:Mo microspheres (c,d), respectively.

https://dx.doi.org/10.1021/acssuschemeng.0c05067
ACS Sustainable Chem. Eng. 2020, 8, 14557−14567

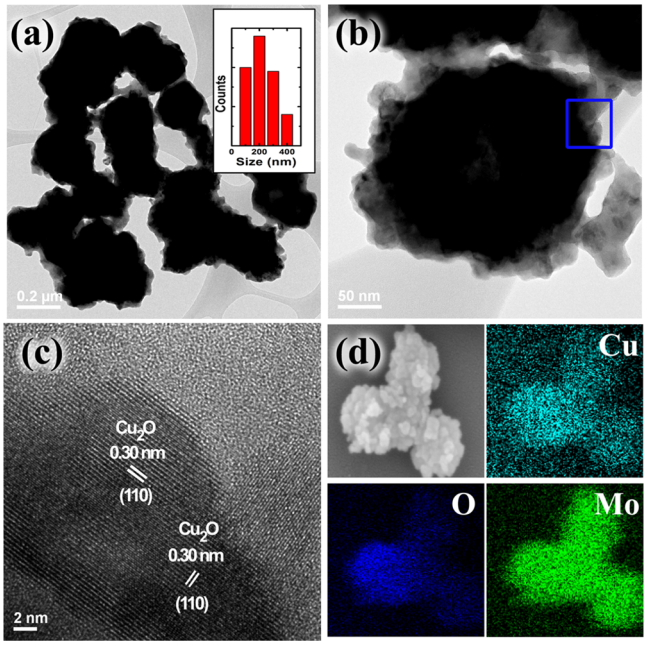

Figure 4. Typical (a) low- and (b) high-magnification TEM image, (c) HR-TEM image taken over the region marked by the blue square in (b), and (d) EDS-elemental mapping images of the Cu_2O:Mo microspheres.

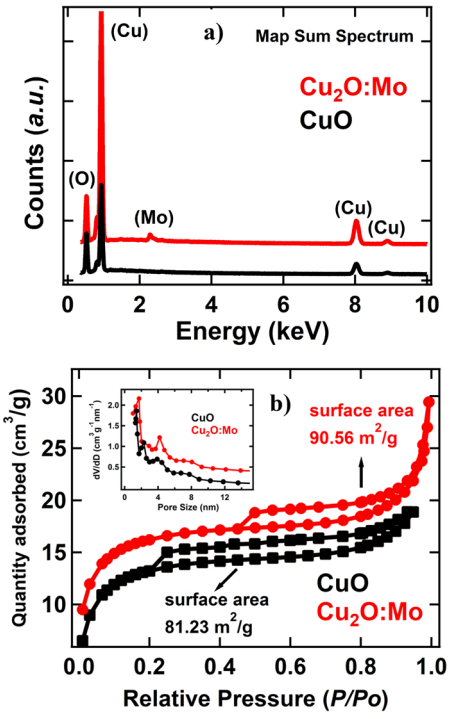

Figure 5. Typical (a) EDS spectra and (b) N_2 adsorption−desorption isotherms of the pristine CuO and porous Cu_2O:Mo microspheres. BJH estimated pore size distributions in the samples are presented as inset of b).

and O signals form the Cu_2O:Mo sample without any additional signals. The estimated Mo content in the microspheres from the EDS-spectrum analysis was about 4.32 wt % (Figure 5a).

Nitrogen (N_2) adsorption−desorption isotherms of the fabricated microspheres were recorded at 77 K to estimate their specific surface area (SSA). As shown in Figure 5b, both the samples revealed typical IV isotherms with H_3-type hysteresis loops in the 0.1−1.0 relative pressure range, suggesting their mesoporous nature. As can be noticed, the shape of the adsorption- desorption hysteresis of the Cu_2O:Mo microsphere sample is a bit different from the pristine CuO microsphere sample, probably due to the difference in their morphology. The Brunauer−Emmett−Teller (BET) estimated SSA of the porous Cu_2O:Mo sample was 90.56 $m^2\ g^{-1}$, which is relatively higher in comparison with the SSA of the pristine CuO microsphere sample (81.23 $m^2\ g^{-1}$). A higher specific surface area of the latter sample could be due to the smaller size (inset of Figure 4a and Figure S3, Supporting Information) of its constituting particles and their porous nature. The estimated SSA of the as-synthesized porous Cu_2O:Mo microsphere sample is much greater than the SSA values reported earlier for the hierarchical CuO hollow microspheres (18.5 $m^2\ g^{-1}$),[54] Cu_2O nanocrystals (38.9 $m^2\ g^{-1}$),[24] and cubic and octahedral Cu_2O nanostructures (12.14, 10.97 m^2g^{-1}),[30] respectively. On the other hand, BJH estimated (using the desorption branch of the isotherm) pore-size distributions of the samples were almost same for Cu_2O:Mo and pristine CuO samples (inset of Figure. 5b), while the average pore size in both the samples was about 4.0 nm.

X-ray photoelectron spectroscopy (XPS) measurements were carried out to understand the chemical composition of the CuO and Cu_2O:Mo samples and valence states of their constituting elements. The XPS survey scans of the pristine CuO, and Cu_2O:Mo samples are shown in Figure 6a. While the emission spectra of the CuO sample revealed signals correspond to Cu and O, the Cu_2O:Mo sample revealed the signals of Cu, O, and Mo. Apart from the signal of residual C, there appeared no additional signal associated with any other element, indicating the compositional purity of the fabricated samples. High-resolution scans of XPS spectra in the Cu 2p and O 1s core-level regions of the pristine CuO sample are displayed in Figure S4 (Supporting Information). The deconvoluted XPS spectra revealed two-component spin−orbit doublets for Cu 2p, peaked around 934 and 953.2 eV, associated with the Cu $2p_{3/2}$ and Cu $2p_{1/2}$ emissions of copper in Cu^{2+} valence state, together with shakeup satellites at 941.0, 943.0, and 962 eV arising because of the electron-correction effects in the open Cu 3d shell ($3d^9$).[55,56] On the other hand, the O 1s core-level emission band of the sample (Figure S4b, Supporting Information) revealed two components at 529.3 and 531.5 eV binding energies (BE), which correspond to surface adsorbed oxygen and copper bound oxygen atoms in CuO, respectively.[44] High-resolution XPS spectra of the Cu_2O:Mo sample recorded in Cu 2p, O 1s, and Mo 3d core-level regions are depicted in Figure 6b−d. As can be noticed in Figure 6b, Cu 2p emission of the Cu_2O:Mo microspheres revealed two components at binding energies of 931.2 and 951.2 eV, which are different from the binding energy values of corresponding emissions from the pristine CuO microspheres, indicating a change in oxidation state of Cu (i.e., from Cu^{2+} to Cu^{+}) in the sample.[57] Notably, no XPS peaks were observed for Cu^0, which could be due to a very low concentration of Cu^0 in the Cu_2O:Mo. Also, the components of the O 1s core-level emission (Figure. 6c) from this sample suffered a small shift of the BE peaks located at 532 and 531 eV for the Cu $2p_{3/2}$ and Cu $2p_{1/2}$, toward higher BE values, suggesting higher oxidation state of Cu. Observed results are in good agreement with the results reported earlier.[57] The Mo 3d

https://dx.doi.org/10.1021/acssuschemeng.0c05067
ACS Sustainable Chem. Eng. 2020, 8, 14557−14567

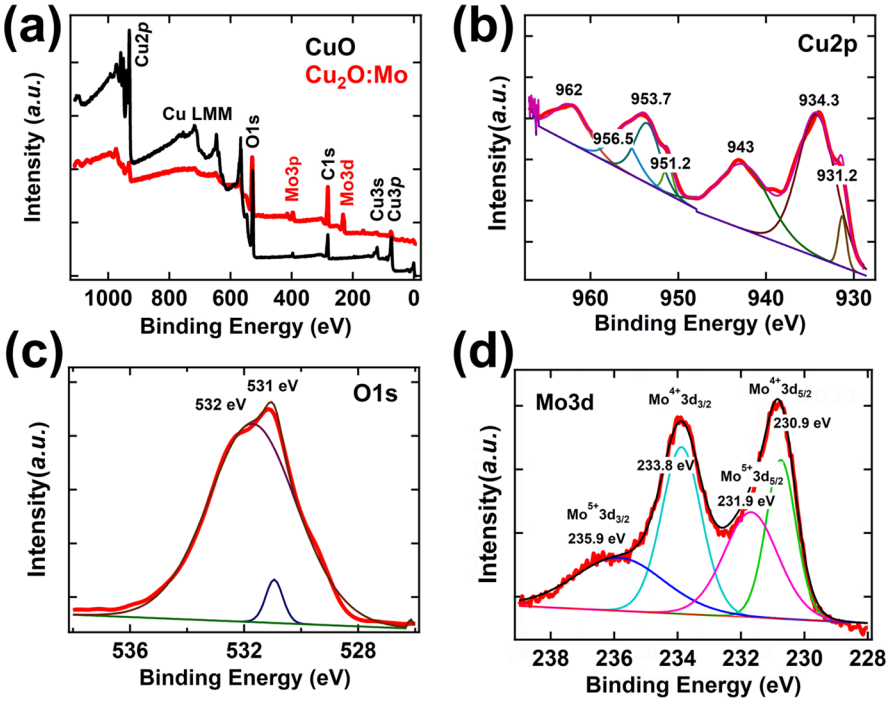

Figure 6. XPS (a) survey spectrum and high-resolution (b) Cu 2p, (c) O 1s, and (d) Mo 3d core-level emissions of Cu_2O:Mo sample. For comparison, the survey spectrum of the pristine CuO sample is included in (a).

region of the XPS spectrum in Figure 6d shows the spin−orbit splitting of 3d orbital into Mo $3d_{5/2}$ and Mo $3d_{3/2}$ core-levels, and these two peaks can be further deconvoluted into two peaks. While the prominent components located around 230.9 and 233.8 eV correspond to the Mo^{4+} oxidation state,[58] the weaker (lower intensity) components peaked around 231.9 and 235.9 eV are attributed to the Mo^{5+} oxidation state.[58,59] The results indicate the Mo incorporated in Cu_2O, remains mainly in Mo^{4+} oxidation state with a minor amount of Mo^{5+}. Quantitative XPS analysis of the sample estimated ∼3.75 wt % of Mo in the microstructures, which is consistent with the Mo content estimated by EDS analysis.

Electrochemical Performance of Cu_2O:Mo Microstructures toward LIBs. The electrochemical Li storage performance of the LIB anode fabricated with porous Cu_2O:Mo microspheres as active material was investigated and compared with the performance of anodes prepared with pristine CuO and CuO_P microspheres. Figure 7 presents the representative CV curves of the porous Cu_2O:Mo microsphere electrodes at a scan rate of 0.1 mV s^{-1} in the potential range 0.01−3.0 V (vs Li^+/Li). The porous Cu_2O:Mo microsphere electrode exhibits two peaks, a sharp peak at 1.64 V, and a broad peak around 0.96 V in the first cathodic cycle corresponds to the lithiation of Cu_2O to form Cu^0 and Li_2O following the electrochemical redox reaction presented in eq 1 and formation of the solid−electrolyte interface (SEI) layer.[60,61] In the subsequent first anodic scan, the high intensity peak at 1.40 V and broad and less intense peaks appeared at 1.71 and 2.30 V are attributed to the decomposition of the organic layer, reoxidation of metallic Cu into Cu_2O, and partial oxidation of Cu_2O into CuO, respectively.[25] In fact, Mo-doping in metal oxide nanostructures is seen to improve their electrical conductivity, surface area, structural stability, and minimize the polarization of Cu_2O, resulting in improved electrochemical conversion

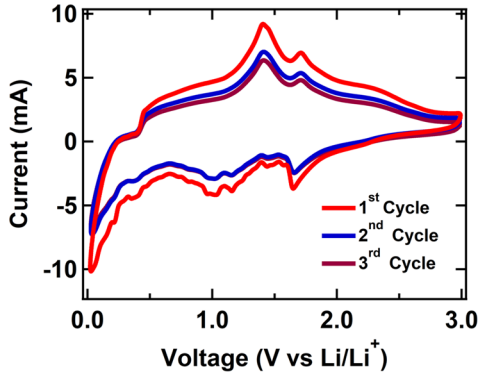

Figure 7. Cyclic voltammogram (CV) curves of 1st, 2nd, and 3rd cycles for porous Cu_2O:Mo microspheres at a sweep rate of 0.1 mV s^{-1} in the potential window 0.01−3.0 V vs Li/Li^+.

reaction reversibility of the Cu_2O:Mo electrode during repeated charging and discharging cycles.[62] The electrochemical reaction between Li^+ ions of the electrolyte and Cu_2O:Mo microspheres electrode proceeds through Li-insertion during the reduction of metal, followed by its reinsertion during the oxidation process,[23] which can be presumed with the following equation:

$$Cu_2O + 2Li^+ + 2e^- \leftarrow\rightarrow Li_2O + 2Cu^0 \quad (1)$$

Figure 8a,b shows the representative galvanostatic charge−discharge curves of the electrodes fabricated with Cu_2O:Mo and CuO microspheres as active anode materials at a current density of 0.1 Ag^{-1} in the voltage range 0.01−3.0 V (vs Li/Li^+). As evidenced in Figure 8a, the galvanostatic charge−discharge curves exhibit multiple plateaus, indicating that the occurrence of multiple conversion reactions between Cu_2O:Mo and lithium ions, which is in accordance with the CV result. The porous Cu_2O:Mo microspheres delivered

https://dx.doi.org/10.1021/acssuschemeng.0c05067
ACS Sustainable Chem. Eng. 2020, 8, 14557−14567

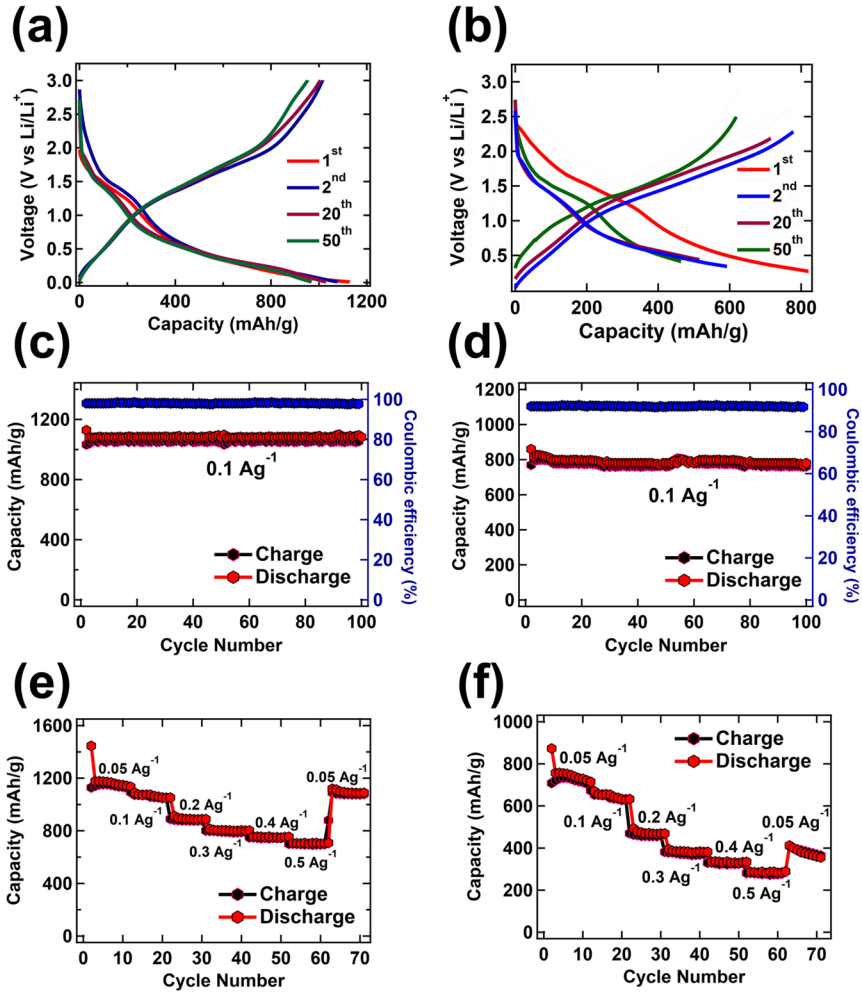

Figure 8. Charge−discharge profiles of (a) Cu_2O:Mo electrodes and (b) CuO electrodes at 0.1 Ag^{-1} current density; (c,d) cycle-stability performance and corresponding Coulombic efficiency at a current density of 0.1 Ag^{-1}; and (e,f) rate capability retention plots under different current densities (0.05−0.5 Ag^{-1}) of the porous Cu_2O:Mo (left column) and pristine CuO electrodes (right column).

discharge capacities of 1128, 1077, 1029, and 969 mAh g^{-1} in the 1st, 2nd, 20th, and 50th cycles, respectively. Discharge capacities of the pristine CuO and CuO_P microsphere electrodes are presented in Figure 8b and Figure S5a (Supporting Information), which showed low charge−discharge capacities and obvious capacity losses. Specifically, the CuO microspheres electrodes (Figure 8b) delivered discharge capacities of 820, 592, 515, 463 mAh g^{-1} and the CuO_P microspheres electrodes (Figure S5a, Supporting Information) delivered discharge capacities of 572, 535, 415, 322 mAh g^{-1} in the 1st, 2nd, 20th, and 50th cycles, respectively. The observed initial discharge capacity values for the pristine CuO microsphere electrode (820 mAh g^{-1}) and Cu_2O:Mo microsphere electrode (1122 mAh g^{-1}) are relatively higher in comparison to the theoretically predicted value of CuO (~674 mAh g^{-1})[60] and Cu_2O (~367 mAh g^{-1}),[23] respectively. The higher discharge capacity of the Cu_2O:Mo microsphere electrode in comparison to the same of the pristine CuO microsphere electrode clearly highlights the effect of Mo doping in Cu_2O. It should be noted that the during the first charge−discharge cycle, a slight irreversible discharge capacity loss occurred, which is due to the electrolyte decomposition and thin SEI layer formation, as observed in several other metal oxide based electrodes.[21,61,63] Moreover, the charge−discharge curves of the repeated cycles (except the first charge−discharge cycle) almost overlapped, indicating much less side reactions and improved contact of Cu_2O:Mo electrode material with the electrolyte, resulting in the formation of very thin SEI layers during the first cycle. The LIBs fabricated using both the Cu_2O:Mo and CuO microsphere electrodes exhibited voltage plateau areas (around 0.75 and 1.5 V, respectively) during charging, generating a major capacity from the anode material.

The cycling stability performance and corresponding Coulombic efficiency (CE) of the porous Cu_2O:Mo and pristine CuO and CuO_P microspheres electrodes were evaluated at a current density of 0.1 Ag^{-1} in the potential window of 0.01−3.0 V as demonstrated in Figure 8c,d and Figure S5b (Supporting Information). The electrode fabricated with Cu_2O:Mo microspheres delivered an initial discharge capacity of 1128 mAh g^{-1} at the first cycle, and it remained stable even after 100 cycles (Figure 8c). The electrode fabricated with Cu_2O:Mo microspheres delivered a much higher reversible capacity of 1082 mAh g^{-1} after 100 cycles with a Coulombic efficiency ~98%, which is significantly higher than that of the electrode made of pristine CuO microspheres (reversible discharge capacity of 89% with Coulombic efficiency of 92%) and the CuO_P microspheres (reversible capacity about 83% with 95% Coulombic efficiency). These results unambiguously confirm that the

https://dx.doi.org/10.1021/acssuschemeng.0c05067
ACS Sustainable Chem. Eng. 2020, 8, 14557−14567

Cu_2O:Mo microsphere anode exhibits the most stable cycling stability, indicating that the Li^+ insertion-extraction process in the anode is highly reversible. The excellent cycling stability could be originated from the good crystallinity and the purity of the Cu_2O:Mo surface, which facilitates a stable SEI layer formation over the surface and high cycling stability during charge-discharging cycles. A typical TEM image of the Cu_2O:Mo electrode material recorded after 100 charge−discharge cycles is presented in Figure S6 (Supporting Information). As is evident, the Cu_2O:Mo microsphere morphology remained almost the same even after the cycling stability test (after 100 charge−discharge cycles), indicating the robust nature of the porous Cu_2O:Mo anode structure, which is the reason for its outstanding cycling stability performance.

Superior rate performance of the porous Cu_2O:Mo microsphere electrodes in LIB was further ascertained by testing them at current densities ranging from 0.05 to 0.5 Ag^{-1}, and their performance was compared with the performance of pristine CuO microsphere electrodes as displayed in Figure 8e,f and Figure S5c (Supporting Information). As can be noticed in Figure 8e, the porous Cu_2O:Mo microspheres at low current density (0.05 Ag^{-1}) delivers a reversible discharge capacity of about 1176 mAh g^{-1}, which decreases to 1089, 913, 815, 755, and 706 mAh g^{-1} on increasing the current density to 0.1, 0.2, 0.3, 0.4, and 0.5 Ag^{-1}, respectively. Notably, even at high current density (0.5 Ag^{-1}), the Cu_2O:Mo microsphere electrode registered a discharge specific capacity of 706 mAh g^{-1}, which is about 60% of the value obtained for 0.1 Ag^{-1} current density. After operating at various current densities, the capacity was almost recovered back about 1089 mAh g^{-1} (about 95%) when returned to the low current density of 0.05 Ag^{-1}, revealing the superior rate capability of the electrode fabricated using Cu_2O:Mo microspheres. However, the electrodes made with pristine CuO and CuO_P microspheres could recover about 47% (Figure 8f) and 24% (Figure S5c, Supporting Information) of their initial capacity when the current density was reversed back to 0.05 Ag^{-1}. Overall, these results demonstrated that the porous Cu_2O:Mo microsphere based electrode exhibits decent reversible capacity recovery after experiencing a high current density of 0.5 Ag^{-1} in comparison with the pristine CuO based electrodes.

Finally, the performance of the electrode made of the Cu_2O:Mo microspheres in LIB has been compared with corresponding literature reported values for the anodes made of Cu_2O-based nanostructures of different morphologies, along with the values reported for other hybrid nanostructures are summarized in Table 1. Since rate performance values can vary depends on mass loading of active material, electrode density, etc., we have compared the initial discharge capacity with the previous literature with similar experimental conditions. One can observe that the anode fabricated using Cu_2O:Mo microspheres fabricated in the present work exhibits a superior discharge capacity, high CE, and decent specific capacity recovery after 100 cycles in comparison with the Cu_2O-nanostructure-based anode electrodes reported so far. The outstanding electrochemical performance, such as highly reversible specific capacity, prolonged cycling stability, and superior rate performance of the anode made of porous Cu_2O:Mo microspheres fabricated in this work, could be due to Mo doping. Mo-doping plays a crucial role on the enhanced Li storage capacity of Cu_2O:Mo microsphere-based electrodes. Specifically, doping of Mo into Cu_2O lattice leads to an enhancement of electrical conductivity, surface area (from 81.23 to 90.56 $m^2\ g^{-1}$), and Li^+ ion transports. A larger surface area of Cu_2O:Mo microsphere electrode provides more active sites and shorter Li^+ ion diffusion length.[55] On the other hand, due to higher ionic radius of Cu^{2+} ions (0.73 Å) than Li^+ ions (0.590 Å)[46] and the porous structure of Cu_2O:Mo microspheres, higher Li^+ ion diffusion occurs in Cu_2O:Mo microspheres, which considerably improves the electrochemical kinetics of lithium ions insertion/extraction. In addition, Mo doping in the Cu_2O lattice also helps to minimize the volume changes upon fast Li^+ ion transport, resulting in enhanced reversible specific capacity and rate performance relative to the pristine CuO microsphere electrodes. Thus, the combination of Mo-doping and the porous structure in the Cu_2O:Mo anode plays a key role in achieving outstanding Li storage capacity and high rate performance of our Cu_2O:Mo-based electrodes.

Table 1. Comparison of Electrochemical Performances of the LIBs Prepared with Porous Cu_2O:Mo Microspheres Electrode with the Literature Reported Performance of LIBs Fabricated with Copper Oxide Based Nano- and Microstructures

nanostructured anode materials	current density	cycle numbers	capacity (mAh g^{-1})	ref
Cu_2O nanocrystals with Cu-vacancies	100 mA g^{-1}	100	1122	23
Cu_2O nanospheres	100 mA g^{-1}	100	650	64
octahedral Cu_2O nanostructures	500 mA g^{-1}	200	569.1	25
Cu_2O−Cu microspheres	50 mA g^{-1}	100	325	65
Cu_2O-GO hollow microspheres	100 mA g^{-1}	50	720	66
Cu_2O/graphene	100 mA g^{-1}	20	424	67
Cu_2O-CuO-TiO_2 hollow nanocages	50 mA g^{-1}	85	700	68
CuO microspheres	100 mA g^{-1}	100	860	this work
porous Cu_2O:Mo microspheres	100 mA g^{-1}	100	1128	this work

Electrochemical impedance spectroscopy (EIS) measurements were performed to further elucidate the electrochemical performance of the pristine CuO, CuO_P, and porous Cu_2O:Mo microspheres electrodes. Figure 9 presents the Nyquist plots of EIS spectra of the electrodes fabricated with CuO, CuO_P, and porous Cu_2O:Mo microspheres. All the

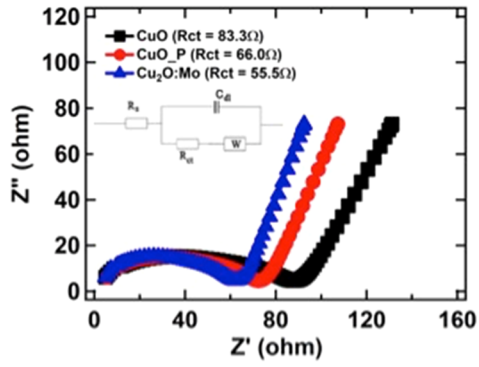

Figure 9. Nyquist plots of as-synthesized CuO (black), CuO_P (red) and the porous Cu_2O: Mo microspheres (blue) along with a probable equivalent circuit (inset).

https://dx.doi.org/10.1021/acssuschemeng.0c05067
ACS Sustainable Chem. Eng. 2020, 8, 14557−14567

three electrodes revealed a semicircle in the high-frequency region, which is the typical Nyquist plot characteristic of a charge-transfer resistance (R_{ct}) at the electrode−electrolyte interface. The long line in the low-frequency side is associated with a combination of kinetic and diffusion resistance of Li^+ ions diffusion in the electrode.[69] As can be seen in Figure 9, while all the cells have very small solution resistance (R_s), the electrode fabricated with Cu_2O:Mo microstructures revealed a semicircle of the smallest diameter, suggesting the lowest R_{ct} at the porous Cu_2O:Mo microstructure−electrolyte interface. The estimated R_{ct} values for the Cu_2O:Mo, CuO, and CuO_P microstructure based electrodes were 55.5, 83.3, and 66.0 Ω, respectively. The lower R_{ct} value for the porous Cu_2O:Mo based electrode clearly indicates a higher electrical conductivity, which is ideal for the LIBs applications.[70] The enhanced conductivity of the porous Cu_2O:Mo microspheres improved the cycling performance of the electrode in LIB. The experimental results obtained in the present study clearly suggest that a combination of Mo doping and porous structural feature of the Cu_2O:Mo microspheres makes them excellent active anode material for Li storage, which can be utilized to fabricate high discharge capacity LIBs with excellent cycling performance.

CONCLUSIONS

In summary, porous Mo-doped Cu_2O microspheres could be successfully fabricated through a green and cost-effective approach using natural *Piper longum* extract as reducing and structure directing agent in combination with hydrothermal treatment. The porous Cu_2O:Mo microspheres bear high specific surface area (90.56 m^2 g^{-1}), higher electrical conductivity, and outstanding structural stability. Fabricated microspheres demonstrate excellent electrochemical performance in LIBs. The LIBs fabricated with anode made of Cu_2O:Mo microspheres registered specific capacity as high as 1128 mAh g^{-1} at current density of 0.1 Ag^{-1}, which is significantly higher than the anodes made of pristine CuO and CuO_P microstructures. The superior performance of the porous Cu_2O:Mo microspheres in LIB is attributed to the combined effect of their porous structure and Mo doping. High specific surface area of the porous Cu_2O:Mo microspheres provides a higher electrode−electrolyte interfacial area, facilitating charge transport at the electrode−electrolyte interface. Moreover, Mo doping enhances the electrical conductivity of the fabricated electrodes, which further improves the charge transfer process at the electrolyte−electrode interface. The green fabrication approach presented in this work is a quite unique and low-cost process, which can be extended for fabricating other functional metal oxide nano/microstructures for application as active anode materials for high-performance energy storage devices.

ASSOCIATED CONTENT

Supporting Information

The Supporting Information is available free of charge at https://pubs.acs.org/doi/10.1021/acssuschemeng.0c05067.

Schematic illustration of synthesis of CuO microspheres, particle size distribution histogram of the CuO microspheres, SEM images along with particle size distribution histogram CuO_P microspheres, XPS analysis, electrochemical performance of CuO_P microspheres in LIBs, and TEM image of the Cu_2O:Mo electrode after 100 discharge−charge cycles (PDF)

AUTHOR INFORMATION

Corresponding Author

Siva Kumar Krishnan − *CONACYT at Instituto de Física, Benemérita Universidad Autónoma de Puebla, Puebla 72570, México;* orcid.org/0000-0002-9672-9335; Email: sivakumar@ifuap.buap.mx

Authors

Paskalis Sahaya Murphin Kumar − *Hydrogen Production Materials Group, National Institute for Material Science, Tsukuba, Ibaraki 305-0044, Japan;* orcid.org/0000-0002-2688-1825

Ala'a H. Al-Muhtaseb − *Department of Petroleum and Chemical Engineering, College of Engineering, Sultan Qaboos University, Muscat 33, Oman;* orcid.org/0000-0003-0114-077X

Gopalakrishnan Kumar − *Institute of Chemistry, Bioscience and Environmental Engineering, Faculty of Science and Technology, University of Stavanger (UiS), 4036 Stavanger, Norway;* orcid.org/0000-0002-7848-5138

Ajayan Vinu − *Global Innovative Center for Advanced Nanomaterials, Faculty of Engineering and Built Environment, The University of Newcastle, Callaghan, New South Wales 2308, Australia;* orcid.org/0000-0002-7508-251X

Wangsoo Cha − *Global Innovative Center for Advanced Nanomaterials, Faculty of Engineering and Built Environment, The University of Newcastle, Callaghan, New South Wales 2308, Australia*

Julio Villanueva Cab − *Instituto de Física, Benemérita Universidad Autónoma de Puebla, Puebla 72570, México;* orcid.org/0000-0002-6261-9197

Umapada Pal − *Instituto de Física, Benemérita Universidad Autónoma de Puebla, Puebla 72570, México;* orcid.org/0000-0002-5665-106X

Complete contact information is available at: https://pubs.acs.org/10.1021/acssuschemeng.0c05067

Notes

The authors declare no competing financial interest.

ACKNOWLEDGMENTS

S.K.K. thanks CONACyT, Mexico, for the help extended through the cathedra of CONACyT project. Financial support extended by VIEP-BUAP and CONACyT (Grant No. CB-2018-A1-S-26720), Mexico, are thankfully acknowledged. The authors are grateful to M. A. Hernandez-Landaverde for technical assistance in the XRD analysis.

REFERENCES

(1) Scrosati, B.; Hassoun, J.; Sun, Y.-K. Lithium-Ion Batteries. A Look into the Future. *Energy Environ. Sci.* **2011**, *4*, 3287−3295.

(2) Gür, T. M. Review of Electrical Energy Storage Technologies, Materials and Systems: Challenges and Prospects for Large-Scale Grid Storage. *Energy Environ. Sci.* **2018**, *11*, 2696−2767.

(3) Cano, Z. P.; Banham, D.; Ye, S.; Hintennach, A.; Lu, J.; Fowler, M.; Chen, Z. Batteries and Fuel Cells for Emerging Electric Vehicle Markets. *Nat. Energy* **2018**, *3*, 279−289.

(4) Dunn, B.; Kamath, H.; Tarascon, J. Electrical Energy Storgae for the Grid: A Battery of Choices. *Science* **2011**, *334*, 928−936.

(5) Choi, N. S.; Chen, Z.; Freunberger, S. A.; Ji, X.; Sun, Y. K.; Amine, K.; Yushin, G.; Nazar, L. F.; Cho, J.; Bruce, P. G. Challenges Facing Lithium Batteries and Electrical Double-Layer Capacitors. *Angew. Chem., Int. Ed.* **2012**, *51*, 9994−1002.
(6) Sun, Y.; Liu, N.; Cui, Y. Promises and Challenges of Nanomaterials for Lithium-Based Rechargeable Batteries. *Nat. Energy* **2016**, *1*, 1−12.
(7) Cai, X.; Lai, L.; Shen, Z.; Lin, J. Graphene and Graphene-Based Composites as Li-Ion Battery Electrode Materials and Their Application in Full Cells. *J. Mater. Chem. A* **2017**, *5*, 15423−15446.
(8) Chabot, V.; Higgins, D.; Yu, A.; Xiao, X.; Chen, Z.; Zhang, J. A Review of Graphene and Graphene Oxide Sponge: Material Synthesis and Applications to Energy and the Environment. *Energy Environ. Sci.* **2014**, *7*, 1564−1596.
(9) Raccichini, R.; Varzi, A.; Passerini, S.; Scrosati, B. The Role of Graphene for Electrochemical Energy Storage. *Nat. Mater.* **2015**, *14*, 271−279.
(10) Reddy, M. V.; Subba Rao, G. V.; Chowdari, B. V. R. Metal Oxides and Oxysalts as Anode Materials for Li Ion Batteries. *Chem. Rev.* **2013**, *113*, 5364−5457.
(11) Wu, F.; Maier, J.; Yu, Y. Guidelines and Trends for Next-Generation Rechargeable Lithium and Lithium-Ion Batteries. *Chem. Soc. Rev.* **2020**, *49*, 1569−1614.
(12) Zang, J.; Ye, J.; Qian, H.; Lin, Y.; Zhang, X.; Zheng, M.; Dong, Q. Hollow Carbon Sphere with Open Pore Encapsulated MnO_2 nanosheets as High-Performance Anode Materials for Lithium Ion Batteries. *Electrochim. Acta* **2018**, *260*, 783−788.
(13) Li, Y.; Ye, D.; Liu, W.; Shi, B.; Guo, R.; Pei, H.; Xie, J. A Three-Dimensional Core-Shell Nanostructured Composite of Polypyrrole Wrapped MnO_2/Reduced Graphene Oxide/Carbon Nanotube for High Performance Lithium Ion Batteries. *J. Colloid Interface Sci.* **2017**, *493*, 241−248.
(14) Kesavan, T.; Boopathi, S.; Kundu, M.; Maduraiveeran, G.; Sasidharan, M. Morphology-Dependent Electrochemical Performance of Spinel-Cobalt Oxide Nanomaterials towards Lithium-Ion Batteries. *Electrochim. Acta* **2018**, *283*, 1668−1678.
(15) Chen, F.; Wang, J.; Huang, L.; Bao, H.; Shi, Y. Ordered Mesoporous Crystalline Mo-Doped WO_2 Materials with High Tap Density as Anode Material for Lithium Ion Batteries. *Chem. Mater.* **2016**, *28*, 608−617.
(16) Guan, Z.; Wang, X.; Li, T.; Zhu, Q.; Jia, M.; Xu, B. Facile Synthesis of Rutile TiO_2/Carbon Nanosheet Composite from MAX Phase for Lithium Storage. *J. Mater. Sci. Technol.* **2019**, *35*, 1977−1981.
(17) Wang, L.; Yue, S.; Zhang, Q.; Zhang, Y.; Li, Y. R.; Lewis, C. S.; Takeuchi, K. J.; Marschilok, A. C.; Takeuchi, E. S.; Wong, S. S. Morphological and Chemical Tuning of High-Energy-Density Metal Oxides for Lithium Ion Battery Electrode Applications. *ACS Energy Lett.* **2017**, *2*, 1465−1478.
(18) Liu, Z.; Yu, Q.; Zhao, Y.; He, R.; Xu, M.; Feng, S.; Li, S.; Zhou, L.; Mai, L. Silicon Oxides: A Promising Family of Anode Materials for Lithium-Ion Batteries. *Chem. Soc. Rev.* **2019**, *48*, 285−309.
(19) Wang, H.-g.; Jiang, C.; Yuan, C.; Wu, Q.; Li, Q.; Duan, Q. Complexing Agent Engineered Strategy for Anchoring SnO_2 nanoparticles on Sulfur/Nitrogen Co-Doped Graphene for Superior Lithium and Sodium Ion Storage. *Chem. Eng. J.* **2018**, *332*, 237−244.
(20) Zhang, L.; Li, Q.; Xue, H.; Pang, H. Fabrication of Cu_2O-Based Materials for Lithium-Ion Batteries. *ChemSusChem* **2018**, *11*, 1581−1599.
(21) Wang, C.; Li, Q.; Wang, F.; Xia, G.; Liu, R.; Li, D.; Li, N.; Spendelow, J. S.; Wu, G. Morphology-Dependent Performance of CuO Anodes via Facile and Controllable Synthesis for Lithium-Ion Batteries. *ACS Appl. Mater. Interfaces* **2014**, *6*, 1243−1250.
(22) Sun, L.; Deng, Q.; Li, Y.; Deng, L.; Wang, Y.; Ren, X.; Zhang, P. Solvothermal Synthesis of Ternary Cu_2O-CuO-RGO Composites as Anode Materials for High Performance Lithium-Ion Batteries. *Electrochim. Acta* **2016**, *222*, 1650−1659.
(23) Song, H.; Gong, Y.; Su, J.; Li, Y.; Li, Y.; Gu, L.; Wang, C. Surfaces/Interfaces Modification for Vacancies Enhancing Lithium Storage Capability of Cu_2O Ultrasmall Nanocrystals. *ACS Appl. Mater. Interfaces* **2018**, *10*, 35137−35144.
(24) Liu, Y.; Zhang, S.; Qin, X.; Kang, F.; Chen, G.; Li, B. In-Plane Highly Dispersed Cu_2O Nanoparticles for Seeded Lithium Deposition. *Nano Lett.* **2019**, *19*, 4601−4607.
(25) Kim, M. C.; Kim, S. J.; Han, S. B.; Kwak, D. H.; Hwang, E. T.; Kim, D. M.; Lee, G. H.; Choe, H. S.; Park, K. W. Cubic and Octahedral Cu_2O Nanostructures as Anodes for Lithium-Ion Batteries. *J. Mater. Chem. A* **2015**, *3*, 23003−23010.
(26) Paolella, A.; Brescia, R.; Prato, M.; Povia, M.; Marras, S.; De Trizio, L.; Falqui, A.; Manna, L.; George, C. Colloidal Synthesis of Cuprite (Cu_2O) Octahedral Nanocrystals and Their Electrochemical Lithiation. *ACS Appl. Mater. Interfaces* **2013**, *5*, 2745−2751.
(27) Kim, E. S.; Kim, M. C.; Moon, S. H.; Shin, Y. K.; Lee, J. E.; Choi, S.; Park, K. W. Surface Modified and Size-Controlled Octahedral Cu_2O Nanostructured Electrodes for Lithium-Ion Batteries. *J. Alloys Compd.* **2019**, *794*, 84−93.
(28) Sun, S.; Zhang, X.; Yang, Q.; Liang, S.; Zhang, X.; Yang, Z. Cuprous Oxide (Cu_2O) Crystals with Tailored Architectures: A Comprehensive Review on Synthesis, Fundamental Properties, Functional Modifications and Applications. *Prog. Mater. Sci.* **2018**, *96*, 111−173.
(29) Uematsu, T.; Miyamoto, Y.; Ogasawara, Y.; Suzuki, K.; Yamaguchi, K.; Mizuno, N. Molybdenum-Doped α-MnO_2 as an Efficient Reusable Heterogeneous Catalyst for Aerobic Sulfide Oxygenation. *Catal. Sci. Technol.* **2016**, *6*, 222−233.
(30) Palmieri, A.; Yazdani, S.; Kashfi-Sadabad, R.; Karakalos, S. G.; Pettes, M. T.; Mustain, W. E. Cobalt Doping as a Pathway to Stabilize the Solid-State Conversion Chemistry of Manganese Oxide Anodes in Li-Ion Batteries. *J. Phys. Chem. C* **2018**, *122*, 7120−7127.
(31) Song, H.; Liu, Y.; Zhang, C.; Liu, C.; Cao, G. Mo-Doped LiV_3O_8 nanorod-Assembled Nanosheets as a High Performance Cathode Material for Lithium Ion Batteries. *J. Mater. Chem. A* **2015**, *3*, 3547−3558.
(32) Song, H.; Kim, Y. T. A Mo-Doped $TiNb_2O_7$ Anode for Lithium-Ion Batteries with High Rate Capability Due to Charge Redistribution. *Chem. Commun.* **2015**, *51*, 9849−9852.
(33) Wang, X.; Li, Z.; Zhang, Z.; Li, Q.; Guo, E.; Wang, C.; Yin, L. Mo-Doped SnO_2 Mesoporous Hollow Structured Spheres as Anode Materials for High-Performance Lithium Ion Batteries. *Nanoscale* **2015**, *7*, 3604−3613.
(34) Świątowska-Mrowiecka, J.; De Diesbach, S.; Maurice, V.; Zanna, S.; Klein, L.; Briand, E.; Vickridge, I.; Marcus, P. Li-Ion Intercalation in Thermal Oxide Thin Films of MoO_3 as Studied by XPS, RBS, and NRA. *J. Phys. Chem. C* **2008**, *112*, 11050−11058.
(35) Kuo, C. H.; Huang, M. H. Morphologically Controlled Synthesis of Cu_2O Nanocrystals and Their Properties. *Nano Today* **2010**, *5*, 106−116.
(36) Clarke, C. J.; Tu, W. C.; Levers, O.; Bröhl, A.; Hallett, J. P. Green and Sustainable Solvents in Chemical Processes. *Chem. Rev.* **2018**, *118*, 747−800.
(37) Shankar, P. D.; Shobana, S.; Karuppusamy, I.; Pugazhendhi, A.; Ramkumar, V. S.; Arvindnarayan, S.; Kumar, G. A Review on the Biosynthesis of Metallic Nanoparticles (Gold and Silver) Using Bio-Components of Microalgae: Formation Mechanism and Applications. *Enzyme Microb. Technol.* **2016**, *95*, 28−44.
(38) Muthukumaran, M.; Niranjani, S.; Barnabas, K. S.; Narayanan, V.; Raju, T.; Venkatachalam, K. Green Route Synthesis and Characterization of Cuprous Oxide (Cu_2O): Visible Light Irradiation Photocatalytic Activity of MB Dye. *Mater. Today Proc.* **2019**, *14*, 563−568.
(39) Nasrollahzadeh, M.; Mohammad Sajadi, S.; Maham, M.; Ehsani, A. Facile and Surfactant-Free Synthesis of Pd Nanoparticles by the Extract of the Fruits of Piper Longum and Their Catalytic Performance for the Sonogashira Coupling Reaction in Water under Ligand- and Copper-Free Conditions. *RSC Adv.* **2015**, *5*, 2562−2567.
(40) Tammina, S. K.; Mandal, B. K.; Ranjan, S.; Dasgupta, N. Cytotoxicity Study of Piper Nigrum Seed Mediated Synthesized SnO_2

https://dx.doi.org/10.1021/acssuschemeng.0c05067
ACS Sustainable Chem. Eng. 2020, 8, 14557−14567

Nanoparticles towards Colorectal (HCT116) and Lung Cancer (A549) Cell Lines. *J. Photochem. Photobiol., B* **2017**, *166*, 158−168.
(41) Kumar, S.; Kamboj, J.; Suman; Sharma, S. Overview for Various Aspects of the Health Benefits of Piper Longum Linn. Fruit. *JAMS J. Acupunct. Meridian Stud.* **2011**, *4*, 134−140.
(42) Sunila, E. S.; Kuttan, G. Immunomodulatory and Antitumor Activity of Piper Longum Linn. and Piperine. *J. Ethnopharmacol.* **2004**, *90*, 339−346.
(43) Jacob, S. J. P.; Mohammed, H.; Murali, K.; Kamarudeen, M. Synthesis of Silver Nanorods Using Coscinium Fenestratum Extracts and Its Cytotoxic Activity against Hep-2 Cell Line. *Colloids Surf., B* **2012**, *98*, 7−11.
(44) Mishra, A. K.; Nayak, A. K.; Das, A. K.; Pradhan, D. Microwave-Assisted Solvothermal Synthesis of Cupric Oxide Nanostructures for High-Performance Supercapacitor. *J. Phys. Chem. C* **2018**, *122*, 11249−11261.
(45) Zheng, J. Y.; Van, T. K.; Pawar, A. U.; Kim, C. W.; Kang, Y. S. One-Step Transformation of Cu to Cu_2O in Alkaline Solution. *RSC Adv.* **2014**, *4*, 18616−18620.
(46) Shannon, R. D. Revised Effective Ionic Radii and Systematic Studies of Interatomie Distances in Halides and Chaleogenides BY. *Acta Crystallogr., Sect. A: Cryst. Phys., Diffr., Theor. Gen. Crystallogr.* **1976**, *32*, 751−767.
(47) Lv, W.; Li, L.; Meng, Q.; Zhang, X. Molybdenum-Doped CuO Nanosheets on Ni Foams with Extraordinary Specific Capacitance for Advanced Hybrid Supercapacitors. *J. Mater. Sci.* **2019**, *55*, 2492−2502.
(48) Balaghi, S. E.; Triana, C. A.; Patzke, G. R. Molybdenum-Doped Manganese Oxide as a Highly Efficient and Economical Water Oxidation Catalyst. *ACS Catal.* **2020**, *10*, 2074−2087.
(49) Wang, M. Y.; Wang, X. L.; Yao, Z. J.; Xie, D.; Xia, X. H.; Gu, C. D.; Tu, J. P. Molybdenum-Doped Tin Oxide Nanoflake Arrays Anchored on Carbon Foam as Flexible Anodes for Sodium-Ion Batteries. *J. Colloid Interface Sci.* **2020**, *560*, 169−176.
(50) Wang, W.Z.; Wang, G.H.; Wang, X.S.; Zhan, Y.J.; Liu, Y.K.; Zheng, C.L. Synthesis and Characterization of Cu_2O Nanowires by a Novel Reduction Route. *Adv. Mater.* **2002**, *14*, 67−69.
(51) Zhao, Y. F.; Yang, Z. Y.; Zhang, Y. X.; Jing, L.; Guo, X.; Ke, Z.; Hu, P.; Wang, G.; Yan, Y. M.; Sun, K. N. Cu_2O Decorated with Cocatalyst MoS_2 for Solar Hydrogen Production with Enhanced Efficiency under Visible Light. *J. Phys. Chem. C* **2014**, *118*, 14238−14245.
(52) Wang, A. J.; Feng, J. J.; Li, Z. H.; Liao, Q. C.; Wang, Z. Z.; Chen, J. R. Solvothermal Synthesis of Cu/Cu_2O Hollow Microspheres for Non-Enzymatic Amperometric Glucose Sensing. *CrystEngComm* **2012**, *14*, 1289−1295.
(53) Hua, Q.; Cao, T.; Gu, X. K.; Lu, J.; Jiang, Z.; Pan, X.; Luo, L.; Li, W. X.; Huang, W. Crystal-Plane-Controlled Selectivity of Cu_2O Catalysts in Propylene Oxidation with Molecular Oxygen. *Angew. Chem., Int. Ed.* **2014**, *53*, 4856−4861.
(54) Wang, J.; Liu, Y.; Wang, S.; Guo, X.; Liu, Y. Facile Fabrication of Pompon-like Hierarchical CuO Hollow Microspheres for High-Performance Lithium-Ion Batteries. *J. Mater. Chem. A* **2014**, *2*, 1224−1229.
(55) Yin, D.; Huang, G.; Na, Z.; Wang, X.; Li, Q.; Wang, L. CuO Nanorod Arrays Formed Directly on Cu Foil from MOFs as Superior Binder-Free Anode Material for Lithium-Ion Batteries. *ACS Energy Lett.* **2017**, *2*, 1564−1570.
(56) Wu, S.; Fu, G.; Lv, W.; Wei, J.; Chen, W.; Yi, H.; Gu, M.; Bai, X.; Zhu, L.; Tan, C.; Liang, Y.; Zhu, G.; He, J.; Wang, X.; Zhang, K. H. L.; Xiong, J.; He, W. A Single-Step Hydrothermal Route to 3D Hierarchical Cu_2O/CuO/RGO Nanosheets as High-Performance Anode of Lithium-Ion Batteries. *Small* **2018**, *14*, 1702667−1702675.
(57) Pawar, S. M.; Kim, J.; Inamdar, A. I.; Woo, H.; Jo, Y.; Pawar, B. S.; Cho, S.; Kim, H.; Im, H. Multi-Functional Reactively-Sputtered Copper Oxide Electrodes for Supercapacitor and Electro-Catalyst in Direct Methanol Fuel Cell Applications. *Sci. Rep.* **2016**, *6*, 21310−21319.
(58) Orozco, C.; Melendez, A.; Manadhar, S.; Singamaneni, S. R.; Reddy, K. M.; Gandha, K.; Niebedim, I. C.; Ramana, C. V. Effect of Molybdenum Incorporation on the Structure and Magnetic Properties of Cobalt Ferrite. *J. Phys. Chem. C* **2017**, *121*, 25463−25471.
(59) Choi, J. G.; Thompson, L. T. XPS Study of As-Prepared and Reduced Molybdenum Oxides. *Appl. Surf. Sci.* **1996**, *93*, 143−149.
(60) Chen, K.; Xue, D.; Komarneni, S. Beyond Theoretical Capacity in Cu-Based Integrated Anode: Insight into the Structural Evolution of CuO. *J. Power Sources* **2015**, *275*, 136−143.
(61) Huang, Q.; Wei, T.; Zhang, M.; Dong, L. Z.; Zhang, A. M.; Li, S. L.; Liu, W. J.; Liu, J.; Lan, Y. Q. A Highly Stable Polyoxometalate-Based Metal-Organic Framework with π-π Stacking for Enhancing Lithium Ion Battery Performance. *J. Mater. Chem. A* **2017**, *5*, 8477−8483.
(62) Dong, Y.; Duan, H.; Park, K. S.; Zhao, Y. Mo^{6+} Doping in Li_3VO_4 Anode for Li-Ion Batteries: Significantly Improve the Reversible Capacity and Rate Performance. *ACS Appl. Mater. Interfaces* **2017**, *9*, 27688−27696.
(63) Wang, H.; Hamanaka, S.; Nishimoto, Y.; Irle, S.; Yokoyama, T.; Yoshikawa, H.; Awaga, K. In Operando X-Ray Absorption Fine Structure Studies of Polyoxometalate Molecular Cluster Batteries: Polyoxometalates as Electron Sponges. *J. Am. Chem. Soc.* **2012**, *134*, 4918−4924.
(64) Shilpa; Rai, P.; Sharma, A. Li-Ion Storage in Morphology Tailored Porous Hollow Cu_2O Nanospheres Fabricated Fabricated by Ostwald Ripening. *RSC Adv.* **2016**, *6*, 105231−105238.
(65) Zhou, H.; Zhao, H.; Zhang, X.; Cheng, H.; Lu, X.; Xu, Q. Facile One-Step Synthesis of Cu_2O@Cu Sub-Microspheres Composites as Anode Materials for Lithium Ion Batteries. *J. Mater. Sci. Technol.* **2018**, *34*, 1085−1090.
(66) Xu, Y. T.; Guo, Y.; Li, C.; Zhou, X. Y.; Tucker, M. C.; Fu, X. Z.; Sun, R.; Wong, C. P. Graphene Oxide Nano-Sheets Wrapped Cu_2O Microspheres as Improved Performance Anode Materials for Lithium Ion Batteries. *Nano Energy* **2015**, *11*, 38−47.
(67) Zhang, Y.; Wang, X.; Zeng, L.; Song, S.; Liu, D. Green and Controlled Synthesis of Cu2O-Graphene Hierarchical Nanohybrids as High-Performance Anode Materials for Lithium-Ion Batteries via an Ultrasound Assisted Approach. *Dalt. Trans.* **2012**, *41*, 4316−4319.
(68) Wang, G.; Sui, Y.; Zhang, M.; Xu, M.; Zeng, Q.; Liu, C.; Liu, X.; Du, F.; Zou, B. One-Pot Synthesis of Uniform Cu_2O-CuO-TiO_2 Hollow Nanocages with Highly Stable Lithium Storage Properties. *J. Mater. Chem. A* **2017**, *5*, 18577−18584.
(69) Liu, Y.; Wang, W.; Gu, L.; Wang, Y.; Ying, Y.; Mao, Y.; Sun, L.; Peng, X. Flexible CuO Nanosheets/Reduced-Graphene Oxide Composite Paper: Binder-Free Anode for High-Performance Lithium-Ion Batteries. *ACS Appl. Mater. Interfaces* **2013**, *5*, 9850−9855.
(70) Cao, Y.; Yang, Y.; Ren, Z.; Jian, N.; Gao, M.; Wu, Y.; Zhu, M.; Pan, F.; Liu, Y.; Pan, H. A New Strategy to Effectively Suppress the Initial Capacity Fading of Iron Oxides by Reacting with $LiBH_4$. *Adv. Funct. Mater.* **2017**, *27*, 1700342−170354.

https://dx.doi.org/10.1021/acssuschemeng.0c05067
ACS Sustainable Chem. Eng. 2020, 8, 14557−14567